

Growth of thick [1 1 1]-oriented 3C-SiC films on T-shaped Si micropillars

M. Agati^{a,*}, S. Boninelli^a, C. Calabretta^a, F. Mancarella^b, M. Mauceri^c, D. Crippa^c, M. Albani^d, R. Bergamaschini^d, L. Miglio^d, F. La Via^a



^aConsiglio Nazionale delle Ricerche - Istituto per la Microelettronica e i Microsistemi (CNR-IMM), Strada VIII n. 5, 95121 Catania, Italy

^bConsiglio Nazionale delle Ricerche - Istituto per la Microelettronica e i Microsistemi (CNR-IMM), via Gobetti n. 101, 40129 Bologna, Italy

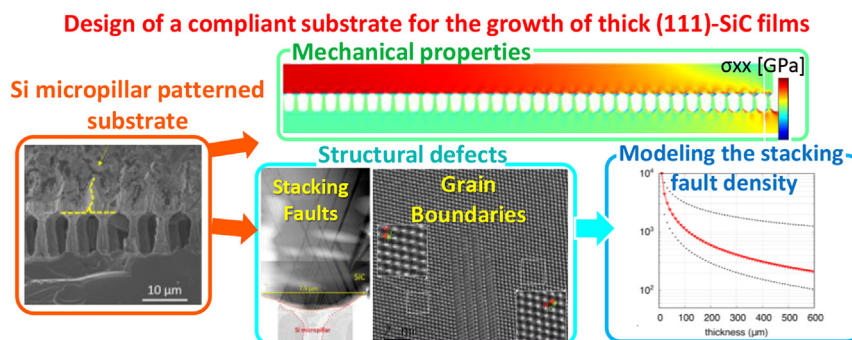
^cLPE, XVI Strada Pantano d'Arce, 95030 Catania, Italy

^dL-NESS and Dipartimento di Scienza dei Materiali, Università di Milano-Bicocca, via R. Cozzi n. 55, 20125 Milano, Italy

HIGHLIGHTS

- We report on the design of a suitable compliant substrate, based on Si micropillars, to grow (1 1 1) 3C-SiC films.
- The new T-shape design of the pillars further improves the strain relaxation, preventing wafer bowing.
- Growth of thick (1 1 1) 3C-SiC films allowed for the first time to study the defects evolution along the [1 1 1] direction.
- Our model estimates that a stacking fault density below $5 \times 10^2 \text{ cm}^{-1}$ could be achieved in 300 μm -thick films.
- We observe and explain the origin of the grain boundary closure in 3C-SiC films grown along the [1 1 1] direction.

GRAPHICAL ABSTRACT



ARTICLE INFO

Article history:

Received 7 April 2021

Accepted 13 May 2021

Available online 15 May 2021

Keywords:

Silicon carbide

Hetero-epitaxy

Compliant substrates

Crystal defects

Atomic resolution scanning transmission

electron microscopy

Finite-element analysis

ABSTRACT

In this paper we report the morphology and the microstructural properties of thick [1 1 1]-oriented 3C-SiC films epitaxially grown on T-shaped Si micropillars. This compliant substrate was designed to release the stress developed in 3C-SiC grown on Si, due to the lattice mismatch and the different thermal expansion coefficients between 3C-SiC and Si. In this way it was possible to have 3C-SiC films as thick as 10 and 16 μm , with small bowing and no cracks. Our study relies on the use of an Electron Microscopy approach and elucidates the structure of the crystallographic defects across the 3C-SiC film, such as stacking faults (SFs), nano-twins and grain boundaries (GBs). After examination of the morphological and structural characteristics of the Si micropillar array, we analyzed the crystallographic properties of the thin 3C-SiC deposit on the Si micropillar sidewalls, since it may have an impact on the upper film. To assess the crystal quality of the 3C-SiC film, we quantified the SF density at the 3C-SiC surface, even estimating semi-quantitatively the depletion of SFs at much larger thickness. Hence, we analyzed the regions where 3C-SiC microcrystals grown on neighboring Si micropillars coalesce and form a continuous layer. We found that the coalescence between adjacent 3C-SiC microcrystals produces twinned regions, which terminate with the formation of GBs. We noticed that SFs may annihilate at the GBs, leading to the SF reduction across the 3C-SiC film. Finally, we observed the closure of the GBs inside the 3C-SiC film, thus improving the crystal quality of its surface. This work endorses the use of Si micropillars as compliant

* Corresponding author at: IMEC, Kapeldreef 75, 3001 Leuven, Italy.

E-mail addresses: marta.agati@ct.infn.it, marta.agati@imec.be (M. Agati).

substrate to grow thick [1 1 1]-oriented 3C-SiC films with good crystal quality and is preliminary to the exploitation of 3C-SiC for high performing microelectronic devices.

© 2021 The Authors. Published by Elsevier Ltd. This is an open access article under the CC BY-NC-ND license (<http://creativecommons.org/licenses/by-nc-nd/4.0/>).

1. Introduction

Silicon Carbide (SiC) represents today one of the foremost materials for power electronics, leading the ongoing transition in automotive industry towards electric-hybrid vehicles [1,2]. In fact, SiC is a wide band gap semiconductor (having band gap from 2.4 eV to 3.2 eV [3]), enabling the fabrication of devices working at high voltage and high power [1–6]. The technological advances of the last decades have opened the market to the exploitation of the hexagonal SiC allotropes, 4H-SiC and 6H-SiC [7–10]. Nonetheless, the cubic SiC allotrope (3C-SiC) presents important advantages with respect to hexagonal SiC. First of all, it can be applied in MOSFETs working in the low voltage range of 600–1200 V, with higher electron mobility and low resistance [11–13]. Moreover, its crystallographic compatibility with Silicon (Si) permits to grow heteroepitaxial 3C-SiC films on Si substrates, leading to take profit of the well-established Si technology and lower the fabrication costs [14]. However, while 4H-SiC films can be grown with good control and crystal quality, the 3C-SiC growth process suffers of serious drawbacks. Primarily, the large lattice mismatch between 3C-SiC and Si (~20% [3]) generates stress at the heterointerface, which is released through the formation of crystallographic defects, such as stacking faults (SFs), dislocations, antiphase domains, twins, inclusions, hillocks, and so on [2,15,16]. In addition, the difference between the thermal expansion coefficients of SiC and Si (~23% at deposition temperature and 8% at room temperature [2]) induces a large stress during the cooling down step, following SiC deposition on Si [17]. Globally, the resulting 3C-SiC films have poor crystal quality and experience wafer cracks and bowing [18]. This issue becomes more critical for the growth of 3C-SiC along the (1 1 1) direction [2]. In this case, the huge tensile stress, which builds up above 1 μm deposition, has prevented the production of (1 1 1) 3C-SiC wafers with large surface area and considerable thickness [19,20]. As a proof of concept, Severino et al. [20] reported on the significantly reduced SF density (about $1.7 \cdot 10^4 \text{cm}^{-1}$ for a 7 μm -thick film) in 3C-SiC films grown on off-axis (1 1 1) Si substrates, but the sample could not relax its strain via defect formation and exhibited severe wafer bowing. It is then desirable to deposit 3C-SiC films with an acceptable level of both bowing and defects density. Since (0 0 1) 3C-SiC surface is highly irregular and makes device processing more difficult [2,21], it is worth exploring new methods leading to the growth of thick (1 1 1) 3C-SiC films. In this regard, previous works investigated the growth of (1 1 1) 3C-SiC via a pendeo epitaxial growth approach [22,23] and selective epitaxy [24]. From the other hand, more recently further attention has been devoted to the study of compliant substrates. This solution aims at engineering substrates with appropriate geometries that may release the stress at the heterointerface. Some examples of compliant substrates are represented by porous Si [25], Silicon-on-Insulator [26,27], SiGe buffer layer [28], patterned substrates such as inverted Si pyramids (ISP) [29] and Si micropillars [30]. In this latter case, the crystal quality depends on a variety of degrees of freedom, such as the pillar shape and their orientation [31].

This work presents a detailed study of the structural and crystallographic properties of 3C-SiC films epitaxially grown on [1 1 1]-oriented T-shaped Si micropillars. During the deposition of 3C-SiC on Si micropillars, individual 3C-SiC microcrystals start growing on top of the hexagonal top-area of the Si micropillars

and develop in 3-D with a multi-faceted morphology, predominantly exhibiting (1 1 1) slanted facets. As the growth proceeds, these microcrystals expand laterally until they touch each other and coalesce. For a typical pillar spacing of the order of 2 μm , coalescence starts after deposition of a few (3–5) μm , while deposition between 10 and 16 μm is fully sufficient to achieve a continuum and planar layer on top of the Si pillars [31]. By a suitable mask design, arranging pillars into patches separated by larger gaps, it is then possible to obtain 3C-SiC continuous layers releasing the thermal stress by means of peripheral pillar tilting, even for thick deposits of the order of tens of micrometers [30]. The growth on pillars is suggested to provide a better 3C-SiC film in terms of crystal quality, showing a lower SF density than the one of the unpatterned flat areas [32]. In this work, a T-shaped pillar with a necking in the stem is presented for the first time, as designed to allow the tilting at reduced height and leading to better decoupling of the film deposited on the top area with respect to the one on the sidewalls, in turn resulting into a higher crystal quality. Our characterization was conducted via an Electron Microscopy (EM) approach and focused on 3C-SiC films with thickness of 10 and 16 μm . Our purpose was aimed at elucidating the structure of the crystallographic defects and evaluate their evolution across the 3C-SiC film. Furthermore, Transmission EM (TEM) cross-section analyses suggested a semi-quantitative modelling for estimating the defect density depletion for large thickness. As a second step of this study, we analyzed the merging of adjacent 3C-SiC microcrystals grown on neighboring Si micropillars, in order to unravel the nature of the grain boundaries (GBs). It is known that GBs generated in 3C-SiC grown on (0 0 1) Si substrate develop in the form of anti-phase boundaries (APBs) [29]. Such GBs correspond to the merging of two SiC domains rotated 180° around the [1 1 0] direction, generating inverted Si-C doublets across the boundaries. For this reason, they are also known as Inverted Domain Boundaries (IDBs) [33]. Atomic Resolution Scanning Transmission EM allowed us to resolve the Si-C doublet and understand whether APBs form or not between coalesced SiC microcrystals. Since both SFs and APBs significantly reduce the device performances [34], it is of paramount importance to perform a detailed structural and crystallographic study of 3C-SiC films before their exploitation in electronic applications.

2. Methods

Four inches Si (1 1 1) on-axis wafers were patterned by means of a three-step procedure: first, a vertical Bosch process to dig the pillars, then one isotropic dry carving to create the under-etching and the necking, finally a few oxidation-stripping cycles to smooth the sidewalls and reduce the hat thickness (see Fig. 1). The pillar top area, hexagonal in shape, is large 5 μm , the pillar height is approximately 10 μm , and the distance between pillar top parts is 2–2.5 μm . The pillar arrays are still hexagonal in shape, 500 μm in diameter, separated by trenches of 5 μm , in order to avoid their merging and mitigate the wafer bowing (see Fig. 1(d)).

3C-SiC growth [35] was carried out via chemical vapor deposition in a horizontal hot-wall reactor as follows: (i) a bake out was performed at 500 °C in high vacuum condition ($\sim 10^{-4}$ mbar); (ii) after a quick etching of the Si surface via H_2 , the temperature is ramped up to 1140 °C and C_2H_4 (ethylene) is introduced in the reaction chamber to activate the carbonization process, which goes

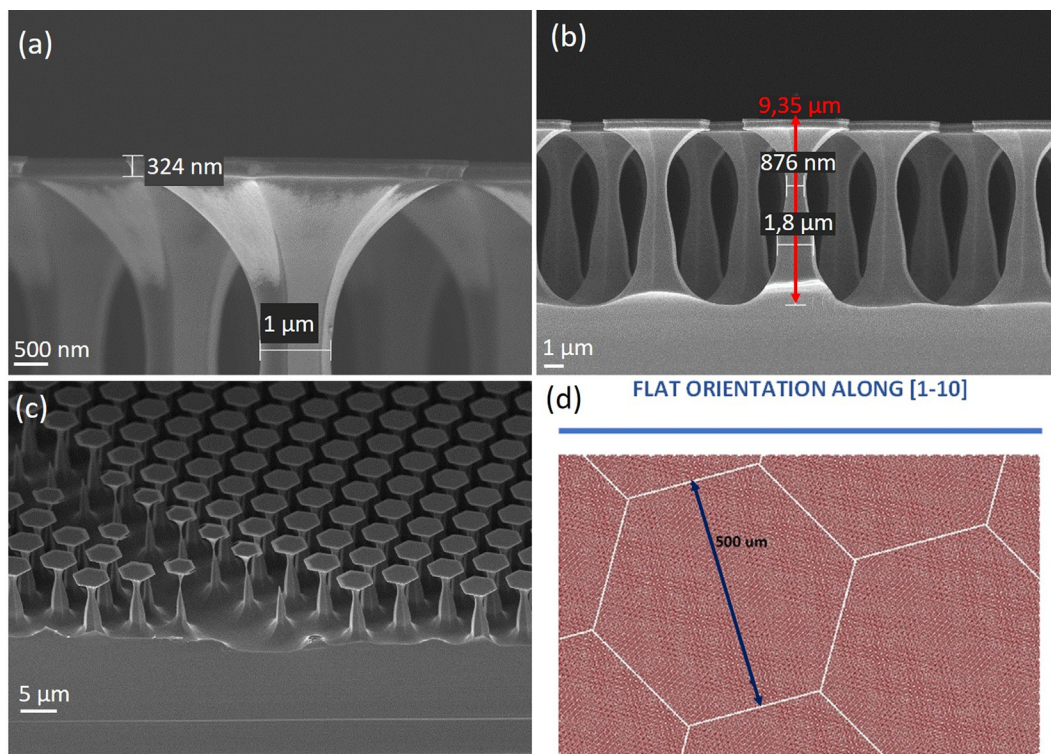


Fig. 1. SEM image of: (a) the micropillar top part after oxide stripping, (b) the full micropillars after isotropic etching, (c) micropillar arrays at the borders of their separation by 5 μm (notice a small nonuniformity in pillar tops). (d) Orientation of the arrays with respect to the flat substrate: 15 and 90° have been tested satisfactorily.

on for 10 min; (iii) the temperature is further increased to 1370 °C, the pressure is set at 100 mbar, and HCl_3Si (trichlorosilane) is inserted together with C_2H_4 to initiate the growth of 3C-SiC. The deposition times were of the order of two to three hours at 6 $\mu\text{m}/\text{hour}$ growth rate, in order to obtain 3C-SiC films having thickness of 10 and 16 μm .

Cross-sectional scanning EM (SEM) allowed us to preliminarily observe the morphological and structural characteristics of the samples. We investigated, via TEM electron diffraction, the characteristics of the thin SiC deposit on the Si micropillar sidewalls, which may have an impact on the crystal properties of the upper SiC film. Then, we analyzed the 3C-SiC film in plan view by SEM, to observe the morphology of the coalesced surface, and by TEM in bright field mode (BF-TEM), to quantitatively evaluate the SF density. To study the SF evolution across the 3C-SiC film, we performed also cross-sectional analyses. In this case, we resorted to a combination of dark field TEM (DF-TEM) and Scanning TEM (STEM) techniques, namely bright field STEM (BF-STEM), medium angle annular dark field STEM and high angle annular dark field STEM (HAADF-STEM). Moreover, atomic resolution HAADF-STEM imaging led us to observe the planar crystallographic defects at atomic scale and to distinguish the atomic structure of SFs, nanotwins and GBs.

We performed SEM imaging by means of a Field Emission SEM Zeiss Supra 25. To perform BF-TEM, DF-TEM imaging and electron diffraction, we used a JEOL JEM 2010F TEM, operating at 200 keV. We also employed a JEOL ARM 200F equipped with a probe aberration corrector (at 200 keV) to perform BF-STEM, medium angle annular DF-STEM and HAADF-STEM imaging up to atomic resolution. To resolve the Si-C doublet, atomic resolution imaging was done decreasing the spot size of the electron probe until reaching the order of magnitude of the Si/C interdistance in the doublet along the $\langle 1\ 1\ 0 \rangle$ zone axis.

3. Results and discussion

3.1. Thermal stress release by T-shaped pillars

It was demonstrated [30] that a substrate patterned with prismatic pillars offers a relevant enhancement in thermal strain relaxation by pillar tilting, particularly important to doctor the problem of wafer bowing in the growth of thick 3C-SiC on $(1\ 1\ 1)$ Si. Here, a new T-shape design of the pillars is introduced to further enhance the strain relaxation, allowing for the growth of thicker layers with limited substrate bowing. The efficacy of this new approach is demonstrated by 2D finite element calculations performed by using COMSOL Multiphysics®.

Fig. 2(a) shows the longitudinal stress component σ_{xx} by color map for a representative geometry of T-shaped pillar array (see Supplementary Part 2 for details). The stress in the 3C-SiC epilayer, originated both by the difference in the thermal expansion coefficients between Si and 3C-SiC and by growth defects, is relaxed thanks to the compliance of the pillar array. This effect is particularly evident at the periphery of the patch because the rotation of the peripheral pillars, which enables the stress relaxation, is more pronounced than the one of the pillars in the middle of the patch. More quantitatively, Fig. 2(b) reports the size of the pillars, i.e. their heights and widths, needed to guarantee a technologically tolerable curvature radius of 10 m. For 4" wafers, this corresponds to an elevation of the wafer borders Δz with respect to the center of the wafer of about 130 μm . This value can be calculated using the average residual strain in the 3C-SiC layer as obtained via simulations, by considering a parabolic bowing for the wafer as $\Delta z = d^2/(8R)$, with d the diameter of the wafer and R the curvature radius in the middle of the wafer (fixed to 10 m) [36]. The comparison with the case of the standard prismatic pillars clearly demonstrates the advantage of the T-shape geometry, which allows for

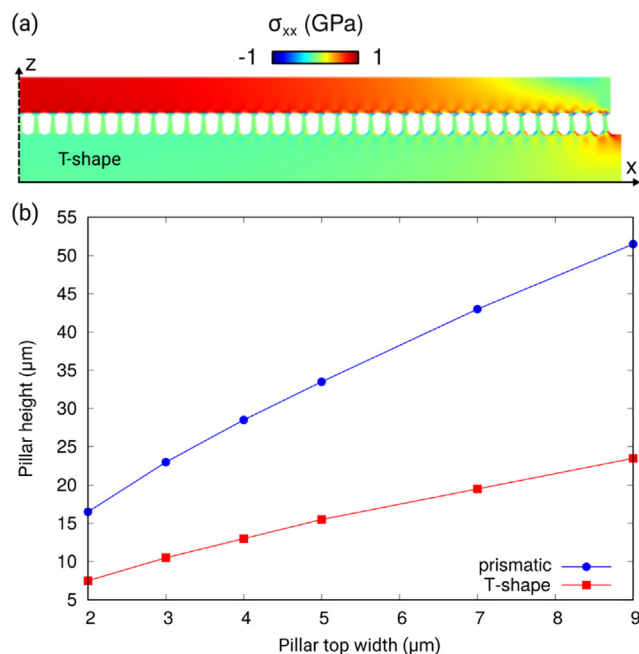


Fig. 2. (a) Color map of the xx component of the stress tensor (σ_{xx}) for a 3C-SiC 500 μm patch (half patch is shown) grown on T-shaped Si pillars on a (1 1 1) substrate. Distance between pillars is 2 μm , pillar base is 5 μm , 3C-SiC thickness is 15 μm . (b) Pillar height, as a function of the pillar top width, required to guarantee a curvature radius greater than 10 m. The patch size is 500 μm and the 3C-SiC thickness is 15 μm . Pillar spacing is 2 μm . The calculation is presented both for standard prismatic pillars and for the T-shaped ones.

shorter pillars at a fixed base. In fact, it is noteworthy that the bowing would be reduced if the experimental T-shaped pillars were as tall as 15 μm (instead of the present 10 μm) and covered the whole wafer (while in current samples the periphery of the wafer was delimited by a circular belt of 1 cm without pillars but with a continuous SiC film, due to technical reasons of the etching mask that can easily be improved). In this case, our SiC samples (with thickness of 10 μm and 16 μm) would have a bowing less than 130 μm , rather than 230 μm and 430 μm , respectively, as measured by focusing the optical microscope at the center and at the borders of the wafer.

3.2. Morphological and structural characteristics of the Si micropillars array

Fig. 3(a) illustrates a SEM image of the sample in cross-section, after deposition of the 3C-SiC film (about 16 μm -thick). The upper SiC film forms after merging of adjacent microcrystals grown on top of neighboring pillars, as indicated by the yellow dashed line. The morphological characteristics of an individual Si micropillar after deposition, in comparison to the ones reported in Fig. 1, are shown more in details in Fig. 3(b). Si micropillars' sidewall appears to be covered by some 200 nm SiC, which forms before the coalescence of the SiC microcrystals laterally expanding from the top of the pillars, at the early stages of the growth. It has been observed that the crystallographic characteristics of the SiC layer deposited on the sidewalls may have an influence on the crystal quality of the upper SiC film. For example, the SiC deposit is polycrystalline in the case of Si micropillars having prismatic shape, with no isotropic etching and no smoothing by oxide stripping. This characteristic is detrimental for the crystal quality of the upper SiC film, which results to have several polycrystalline regions (see Supplementary Part 1, Fig. S1). For this reason, we performed selected area electron diffractions (SAED) along the Si micropillars, as

described in the Supplementary Part 1. The SAED analysis demonstrates that the SiC layer grows epitaxially on the underlying Si pillar sidewalls and presents twin defects. However, we will show in the next sections that the SiC film grows on top of the T-shape Si micropillars with good crystal quality. We concluded that the T-shape of the Si micropillars prevents twin propagation in the upper film. As a matter of fact, twinned regions form in those portions of the SiC film growing between neighboring micropillars, where the coalescence of two adjacent SiC microcrystals occurs.

3.3. Structural analysis of the planar defects in 3C-SiC film

Typical plan view SEM images of the 3C-SiC surface are depicted in Fig. 4(a) and (b), for the 3C-SiC films having thickness of 10 and 16 μm , respectively. These images show some typical triangular islands, that are characteristic of the growth kinetics on the (1 1 1) surface. Moreover, after comparing Fig. 4(a) and (b), we can notice the presence of regularly arranged holes at the surface of the 10 μm -thick sample (corresponding to still unbridged parts of neighboring microcrystals), whilst no hole appears in the 16 μm -thick sample. This observation indicates that the sample achieves full coalescence of the SiC microcrystals after growing 16 μm -thick film [31,32].

The most important remark that can be inferred from the plan view SEM analyses concerns the absence of GBs at the surface. If present, GBs would be easily discerned as they meander randomly along the surface (i.e., they do not lie on a specific plane), separating the single crystalline domains. Similar plan view analyses reported in previous works [29,33] evidenced the presence of GBs emerging up to the surface. In those cases, 3C-SiC growth was performed on planar (0 0 1)-Si surface [33] and on ISP which exposed the four (1 1 1), (1-11), (-1-11), (-1 1 1) facets [29]. It is worth noting at this point that the {1 1 1} surfaces are equivalent for Si, while for 3C-SiC these facets present opposite polarities: while the (1 1 1) and (-1-11) SiC faces expose Si atoms, the (-1 1 1) and (1-11) expose C atoms. In the case of 3C-SiC epitaxial growth on planar (0 0 1)-Si substrate, 3C-SiC nuclei deposited at the early stage of the process align their {1 1 1} surfaces with the {1 1 1} of the Si substrate. Some 3C-SiC nuclei may align their Si-facets or C-facets with equal probability [15]. Further lateral growth and coalescence via Volmer-Weber or Stranski-Krastanov mechanisms lead to the matching of surfaces with opposite polarities and thus to the formation of APB [37]. The existence of APB in 3C-SiC grown on ISP is readily explained by considering that ISP expose the four (1 1 1), (1-1 1), (-1-1 1), (-1 1 1) planes, with adjacent facets having opposite polarities. In this case, the preliminary carbonization step induces the formation of a C-atomic layer on all the four exposed surfaces, generating the anti-phase domains on the adjacent facets [29]. In the case of growth on [1 1 1]-oriented substrates, no APB was detected at the surface. This leads us to suppose that a mechanism of GBs closure exists for our samples, since there are multiple grains generated in correspondence of each Si micropillar that are expected to coalesce forming some sort of GB. This aspect can be investigated via cross-sectional analyses, as discussed in detail in the following section.

Further studies of the 3C-SiC surface were accomplished via plan view TEM imaging, as shown in Fig. 5. In BF mode, i.e., selecting the transmitted spot, it is possible to obtain a better contrast of the SFs at the surface, visible as dark stripes in the image (as indicated by the yellow dashed lines). The inset of Fig. 5 shows the correspondent electron diffraction pattern along the $\langle 1 1 1 \rangle$ zone axis, consistently with the growth along the [1 1 1] direction. In this orientation, since the SFs lie on the {1 1 1}, they appear as stripes lying on the three (-1 1 1), (1-1 1), (1 1-1) planes and form triangular features in the plan view TEM. By performing plan view

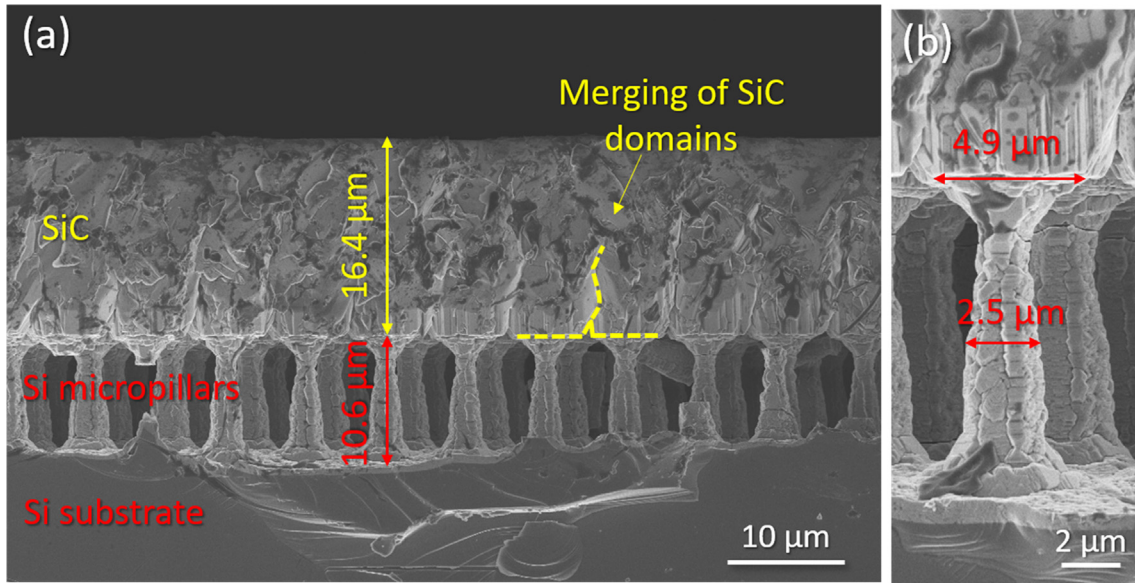


Fig. 3. Cross-sectional SEM image of: (a) the 3C-SiC film grown on Si micropillar patterned substrate and (b) an individual Si micropillar after SiC deposition.

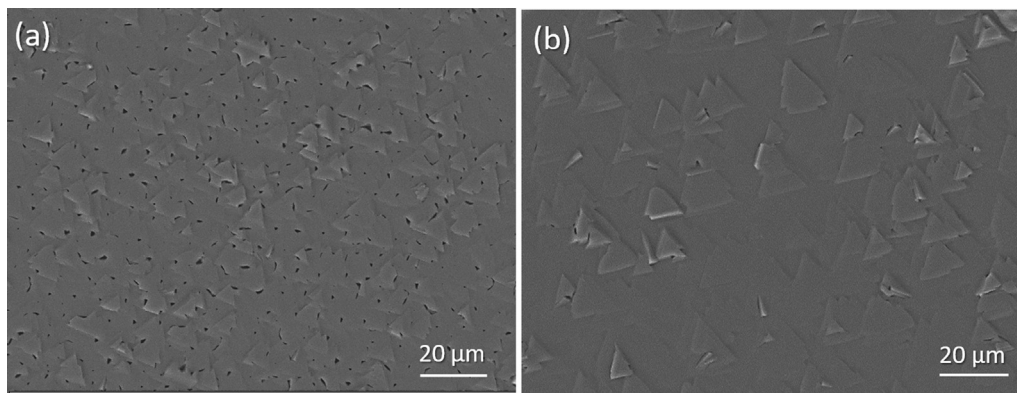


Fig. 4. Plan view SEM images of: (a) 10 μm-thick sample; (b) 16 μm-thick sample.

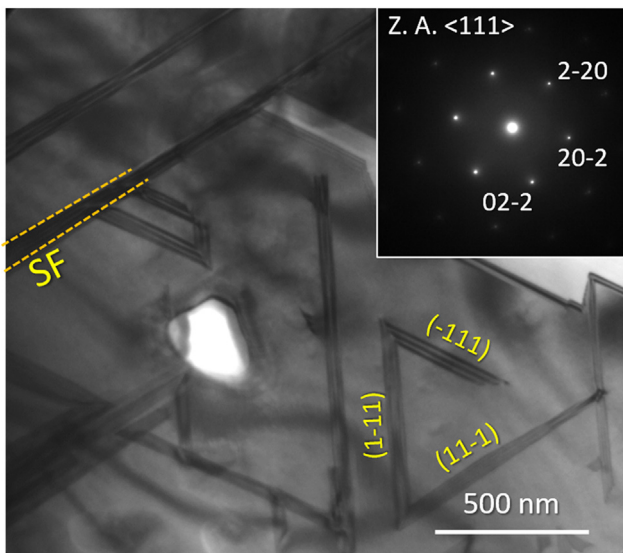


Fig. 5. Plan view BF-TEM image showing the SFs emerging at the surface of 3C-SiC. The corresponding electron diffraction pattern is shown in the inset.

BF-TEM imaging, we statistically evaluated the SF density in the 10 μm-thick sample. To do this, we measured the total length of the SFs in a wide area (~70 μm²), finding that the SF density was ~ 1.7·10⁴ cm⁻¹. This value is in agreement with those found for analogous 3C-SiC films grown on (0 0 1)-Si substrates [14]. Such result is remarkable, since it indicates that 3C-SiC films can be grown also on [1 1 1]-oriented Si with crystal quality comparable with analogous films on [0 0 1]-oriented Si, as long as the use of the compliant substrate mitigates the bowing and allows thicker 3C-SiC films. With this respect, the use of T-shaped pillars is of great benefit, allowing for a significant reduction in the residual thermal stress.

Fig. 6 shows some cross-sectional images of the 3C-SiC film (16 μm-thick) acquired in BF-STEM mode (Fig. 6(a) and (b)) and in medium angle annular DF mode (Fig. 6(c)). In particular, Fig. 6 (b) and (c) depict the same zone of the sample in different STEM modes, corresponding to the region where the merging between adjacent SiC crystals occurs. It is worth noting that the Si micropillars are eliminated during the thinning required for TEM sample preparation. Nonetheless, it is not difficult to infer the position of the Si/SiC interface by observing that the SiC microcrystals growing on top of Si micropillars feature a tulip-shaped morphology. In fact, we observe a series of bulged regions which periodically alternates

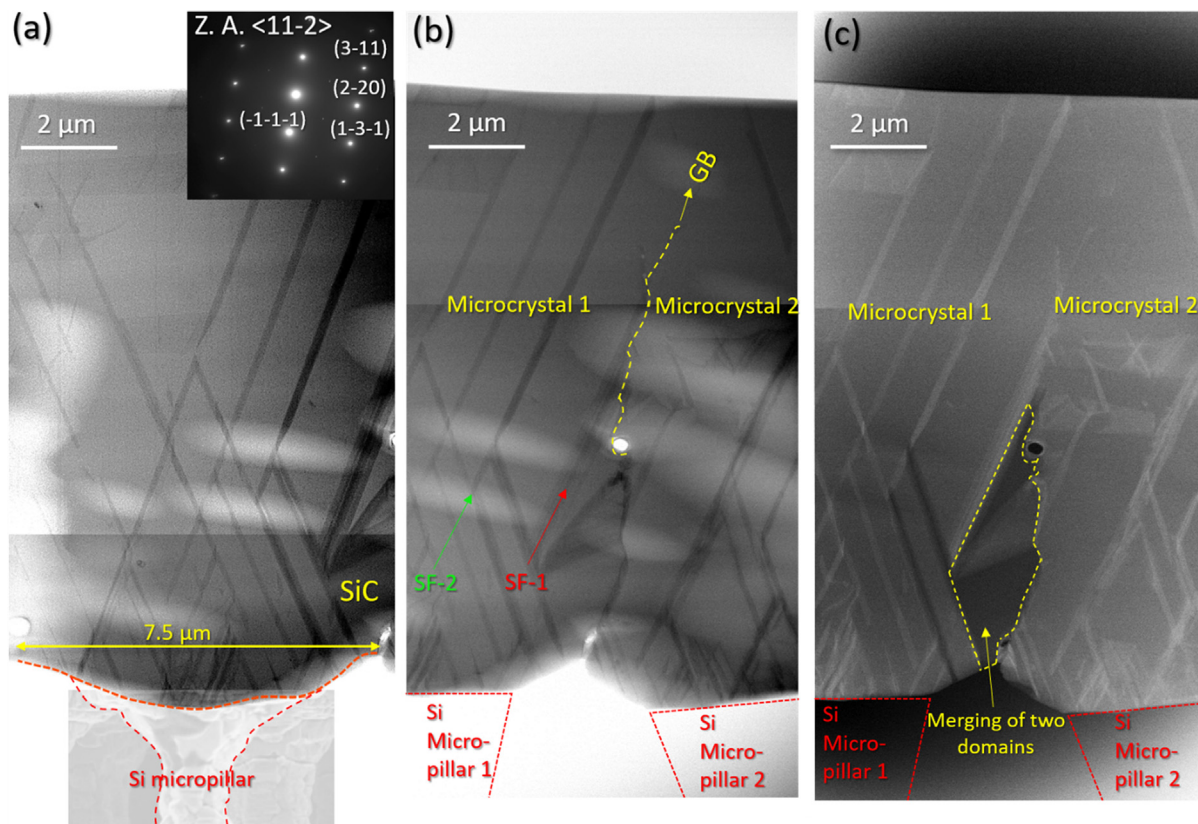


Fig. 6. (a) BF-STEM image of an individual tulip-shaped SiC microcrystal. The SEM image of a Si micropillar, as reported in Figure 3(b), is superimposed to the BF-STEM for the sake of clarity. (b) and (c) depict the region where two adjacent 3C-SiC microcrystals merge in BF-STEM and medium angle annular DF mode, respectively. All these images were acquired along the $\langle 11\bar{2} \rangle$ zone axis, as shown by the electron diffraction in the inset of (a).

with pinched ones; the bulged regions extend for about 7–8 μm and matches very well the profile expected for the SiC microcrystals grown on the Si pillars (which we remind is about 5 μm -large at its top). To make it clearer, in Fig. 6(a), we have indicated the bulged region with the yellow arrow and superimposed, in transparency, the top of the pillar shown in Fig. 3(b). Similarly, the position where the Si micropillars were initially located is also illustrated in Fig. 6(b) and (c).

All these images were acquired along the $\langle 11\bar{2} \rangle$ zone axis, as shown by the electron diffraction in the inset of Fig. 6(a). Along this direction, the SFs are visible as dark stripes, as it is indicated by the arrows in Fig. 6(b). In 3C-SiC the SFs lie on the $\{111\}$ planes and are generated by the misfit between 3C-Si and the underlying (111) Si lattice. It is worth to recall at this point that SFs are planar defects due to an alteration in the sequence of crystallographic planes. Such an alteration may be limited to one single atomic plane or more. In 3C-SiC, the correct stacking sequence is indicated as ABC-ABC(...). We speak about *intrinsic* SF when the stacking sequence lacks one atomic plane, i.e. ABC-AC-ABC. An *extrinsic* SF is given by the insertion of one atomic plane in the sequence, i.e. ABC-ACBC-ABC. When the stacking reproduces the sequence of ABC-ACB-ABC, we refer to this defect as twin (micro- or nanotwin). This defect is equivalent to rotating the crystal by 180° perpendicularly to the A-atomic plane. In other words, this defect separates two crystal regions that are specular between each other. In Fig. 6(b) we have also evidenced the GB via the yellow line. This latter is generated in the region where two neighboring microcrystals coalescence (as indicated in Fig. 6(c)) and prosecutes across the film until it seems to vanish before reaching the surface. This observation further supports the results of the SEM analyses,

which assess the absence of GBs emerging at the surface. The possibility of GBs' closure in 3C-SiC deserves further investigations and will be treated in more detail in the next section. Furthermore, as it can be observed in Fig. 6(b), while the SF indicated by the green line manages to reach the surface, the SF indicated in red crosses the GB and does not continue across the adjacent microcrystal (named "Microcrystal 2" in the same Figure). SF termination at the GBs prevents SF propagation up to the surface and represents a mechanism for SF reduction in 3C-SiC, as previously observed by Zimbone et al. [33]. It is worth to remind, as demonstrated by Zimbone et al. [33], that GB may also generate SFs. However, after several cross-sectional analyses we can conclude that the mechanism of SF generation at the GBs does not significantly contribute to increase the SF density in our samples.

It has been shown, for the $[001]$ growth orientation, that stopping of one SF may happen when crossing another SF, under suitable microscopic conditions [38], with trace in TEM imaging that resembles a λ . Similarly, for the $[111]$ growth orientation one SF moving along one (111) plane can be blocked if two stopping events occur with SFs pertaining to the two other complementary (111) planes, or may proceed with one halved size, if only one blocking event has occurred (see Supplementary Part 3 for further details). A simple counting of the λ events relative to the total number of SF crossings, as observed in the $\{11\bar{2}\}$ TEM cross sections of Fig. 6(a), returns a rough estimate of the stopping probability at each SF intersection of $\eta \approx 35\%$.

The decay of SF density as a function of the deposited thickness can be estimated by a statistical, semi-quantitative model (details are given in the Supplementary Part 3), accounting for the progressive annihilation of SFs due their mutual intersections. For the sake

of simplicity, it is assumed that SFs are all generated at the early stages of 3C-SiC deposition in consequence of the misfit at the interface with Si, neglecting any possible self-nucleation mechanism, eventually entering the parameters fitting in an effective way. The key concept of the model is that, thanks to the lateral discretization imposed by the pillar structure, SFs are grouped in sheafs, as sketched in Fig. 7(a). Then, it is possible to discretize the thickness of the film into slices ($\sim 11 \mu\text{m}$), such that the i -th slice contains all intersections between the SF sheafs from one pillar and those from its i -th neighbors. The probability that SFs continue propagating across each slice is then given by the binomial probability distribution counting SF annihilation at each intersection between all the SFs in the sheafs from the three distinct (1 1 1) planes. In particular, the density of SFs passing through the i -th slice from h_i to h_{i+1} , can be modelled as:

$$\rho(h_{i+1}) = \rho(h_i) \left\{ (1 - \eta)^{\frac{\rho(h_i)L}{2}} + \frac{1}{2} \left[(1 - \eta)^{\frac{\rho(h_i)L}{4}} \cdot \left(2 - (1 - \eta)^{\frac{\rho(h_i)L}{4}} \right) - (1 - \eta)^{\frac{\rho(h_i)L}{2}} \right] \right\} \quad (1)$$

where the first term is the probability that a SF continues propagating in both directions, while the second (i.e., the one in the square brackets) is the probability that it continues only in one direction, being blocked by a λ event in the other. The factor 1/2 is introduced to account for the fact that the SFs propagating in a single direction are more likely to be blocked in the next slice of the film thickness. The variation in SF density as a function of the deposited thickness can be obtained by iterating the calculation of Eq. (1) starting from $\rho(h_1 \approx 11 \mu\text{m}) \approx 10^4 \text{ cm}^{-1}$, resulted from the plan view TEM analysis of the experimental SF density, as discussed above. The result of Eq. (1) is shown by red triangles in Fig. 7(b), while the upper dotted line represents the extreme case when all the partially blocked SFs propagate in the next slice, as if they were not confined in one direction (turn the 1/2 factor to 1 in the second term of Eq. (1)), and the lower dotted line corresponds to the opposite extreme situation, when only the fully integer SFs propagate to the next slice (turn the 1/2 factor to 0 in the second term of Eq. (1)). This simple estimate returns the possibility to achieve a defect density well below $5 \times 10^2 \text{ cm}^{-1}$ at a film thickness of $300 \mu\text{m}$, as reported in Fig. 7(b). This value is very low and close to record values previously found for (0 0 1) 3C-SiC [39].

To complete this paragraph, we present in Fig. 8 some atomic resolution images of the planar defects present in the sample. These images were acquired after aligning the sample along

the (1 1 0) zone axis, in order to observe the edge of the defects. Fig. 8(a) represents the atomic resolution image of a SF formed by a single extra atomic plane (extrinsic SF). The atomic resolution image of a composite nano-twin is also shown in Fig. 8(b), where we can distinguish four crystal regions. We can also notice that region 2 and region 4 have the same crystallographic configurations, being oriented in the same way, as indicated by the cyan lines.

3.4. Merging of adjacent 3C-SiC microcrystals and analysis of the GBs

Fig. 9(a) reports a BF-STEM image of the same region shown in Fig. 6(b) and (c), as observed after tilting towards the (1 1 0) zone axis. The area where the two microcrystals merge and the region of the GB closure are also evidenced. As we said above, since the SFs lie on the {1 1 1} planes, the tilt has the effect to bring one of the SF family on-axis. In Fig. 9(a) we can notice the presence of weakly visible and ultra-thin straight lines in the BF-STEM image, as indicated by the blue arrow. These defects turn to be nano-twins at atomic resolution, as the one shown in Fig. 8(b). The electron diffraction of the sample corresponding to the (1 1 0) zone axis is reported in Fig. 9(b). This diffraction shows not only the pattern of 3C-SiC along the (1 1 0) zone axis, but also some extra-spots that indicate the presence of twinned regions. This statement can be easily justified, if we consider that this diffraction is specular with respect to the (1 1 1) direction. If we perform DF-TEM imaging by selecting one of these spots via the objective aperture in TEM, we can easily discern the twinned regions. Fig. 9(c) show a DF-TEM image corresponding to the region of Fig. 9(a) marked by the red circle. This image shows not only the presence of nano-twins, but more importantly leads us to conclude that the region of merging is also twinned.

This observation deserves further investigations. In this regard, we performed sequential DF-TEM images to catch all the extension of this twinned region. These images are reported in Fig. 10. Here, we can see that the twinned region extends up to 4–5 μm and is recovered before the formation of the GB. By performing further DF-TEM images of the regions of merging, we found that these latter are always twinned and correspond to dark regions in the BF-STEM images acquired in correspondence of the pinched regions.

More importantly, by performing HAADF-STEM at atomic resolution, we managed to unravel the nature of the GBs. By employing a narrower probe size, we were able to resolve the Si-C doublets

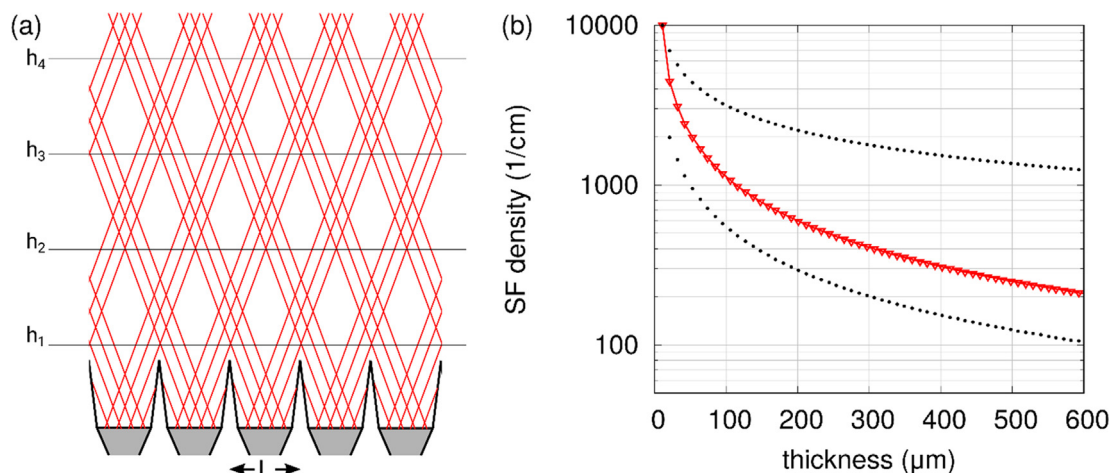


Fig. 7. (a) Schematics of the sheafs of SF planes propagating from each pillar and discretization of the growth thickness into h_i slices, each containing intersections between SFs from i -th neighboring pillars. The lateral periodicity is equal to L . (b) Plot of the variation of SF density as a function of the thickness of the SiC suspended layer. Red triangles show the result of Eq. (1). The dotted lines represent the upper and lower bound limits of Eq. (1). (For interpretation of the references to color in this figure legend, the reader is referred to the web version of this article.)

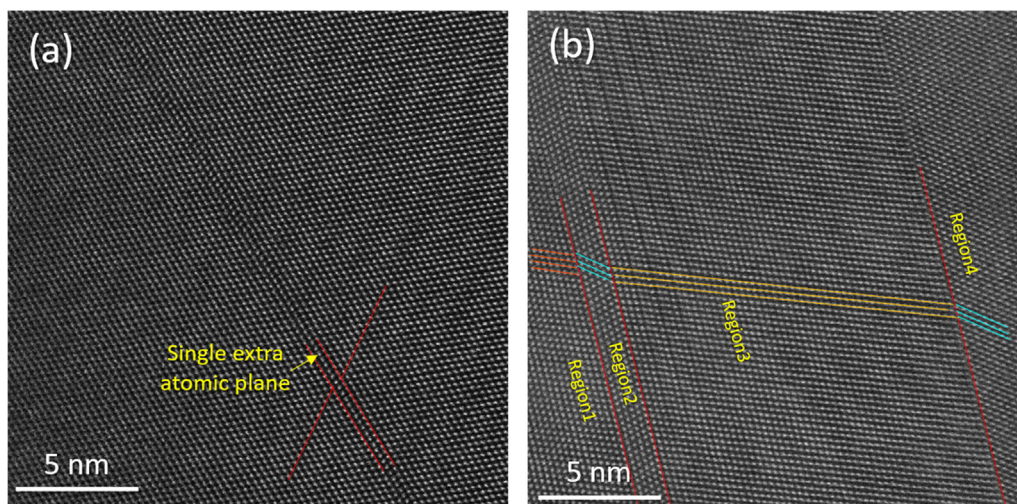


Fig. 8. Atomic resolution images of (a) an extrinsic SF and (b) a nanotwin.

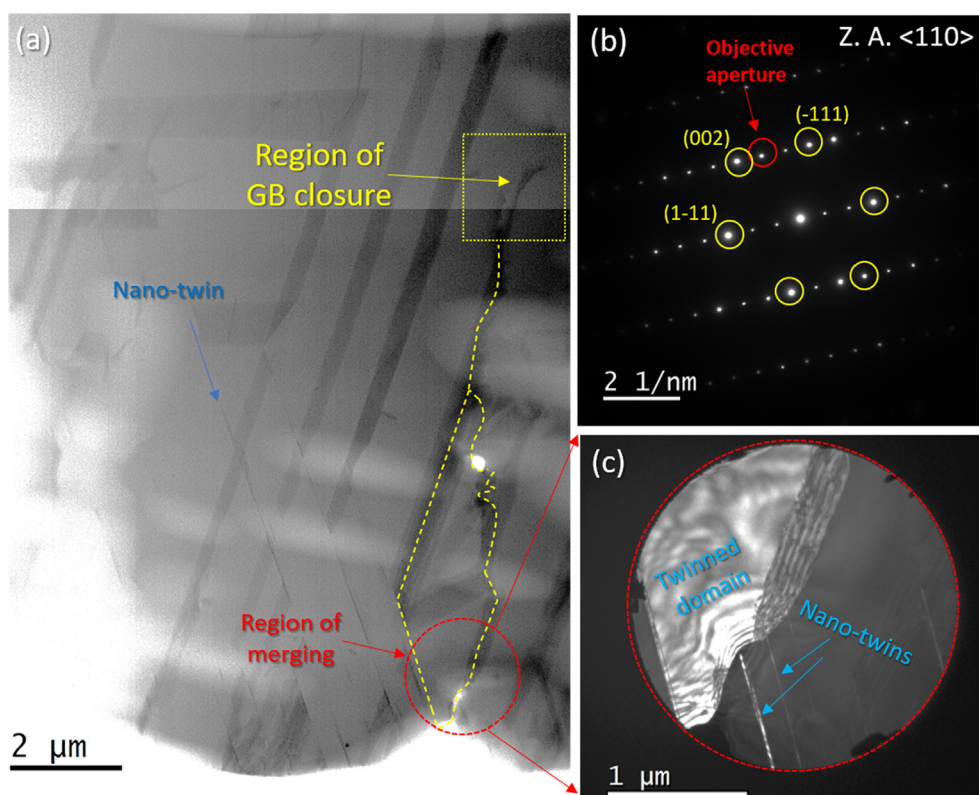


Fig. 9. (a) BF-STEM image of the region where two adjacent microcrystals merge, forming a twinned region terminating with a GB. (b) SAED acquired in correspondence of the region indicated in (a) by the red circle. (c) DF image acquired by selecting the spot indicated in (b) by the red circle. (For interpretation of the references to color in this figure legend, the reader is referred to the web version of this article.)

and understand their orientation on the two sides of the boundary. Fig. 11(a) is acquired in the zone of the GB closure, indicated in Fig. 11(b) by the yellow arrow. As a first remark, we can notice that the orientation of the doublet is the same on the left and on the right of the GB, suggesting that its nature is different from the APB. This fact is strictly related to the growth along the $[1\ 1\ 1]$ direction. In fact, as we said in one of the previous sections, during SiC deposition on the $(0\ 0\ 1)$ -Si substrate, 3C-SiC nuclei have equal probabilities to align their $\{1\ 1\ 1\}$ Si-facets or C-facets with the

$\{1\ 1\ 1\}$ -surfaces of the Si substrate. Then, coalescence of grains may give rise to APB as long as surfaces with opposite polarities face each other.

On the $(1\ 1\ 1)$ -Si surface, as we infer from Fig. 11(a), the formation of antiphase domains does not occur. In fact, along the $[1\ 1\ 1]$ growth direction there are only two possibilities for the Si-C doublet to bond to the Si substrate. We can more easily understand this fact by considering that Si and C atoms in SiC form tetrahedra with one C atom bonded with four Si atoms, or vice versa [40]. The

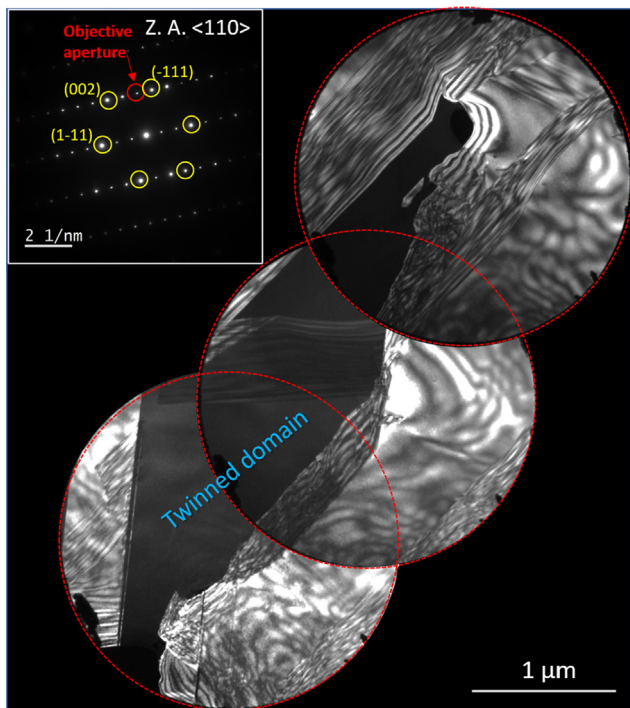


Fig. 10. Sequential DF-TEM images acquired along the region of merging between adjacent 3C-SiC microcrystals. These images are acquired by selecting the spot indicated by the red circle in the SAED displayed as inset. (For interpretation of the references to color in this figure legend, the reader is referred to the web version of this article.)

two possible stacking configurations along the $[1\ 1\ 1]$ growth direction differ just because the SiC tetrahedra are rotated 180° with respect to the $[1\ 1\ 1]$ axis, forming twins and not anti-phase

domains. This reason also explains why the formation of twins is favored in $[1\ 1\ 1]$ -oriented SiC films, as we have seen in the TEM and STEM images all along this paper. The 3C-SiC film may eventually develop SFs during the early stage of the growth. This defect separates crystal regions via the lacking or the addition of atomic planes. It is worth noting that the same crystallographic configuration may be restored after repetitive SFs and twins: this occurred, for example, in Fig. 8(b), where crystal regions with the same orientations (represented by the cyan lines) are interspersed near each other. The same crystallographic configuration may also form in two different 3C-SiC microcrystals, independently growing on neighboring Si micro-pillars. There is a certain number of SFs and nano-twins which separate such equivalent crystal regions. This phenomenon is depicted in the pictorial view shown in Fig. 11(c), where the different crystallographic configurations in two adjacent SiC microcrystals are represented by colored dashed lines in proximity of the GB. When two equivalent crystal configurations merge, as represented by the cyan dashed line in Fig. 11(c), there is no physical reason for the existence of any GB. At this point, we conclude that the closure of the GB occurs.

4. Conclusions

In conclusion, this work demonstrates that T-shaped, $[1\ 1\ 1]$ -oriented Si micropillar arrays provide an effective compliant substrate for the growth of 3C-SiC. Indeed, while the 3C-SiC exhibits good crystal quality, having SF density comparable with those found in analogous 3C-SiC films grown on $(0\ 0\ 1)$ -Si, and no APB, the samples do not present any remarkable wafer bowing. The stress is efficiently released by the tilting of the micropillars, that is effective even for a pillar height as small as $\sim 10\ \mu\text{m}$, due to the necking in the stem. Moreover, both SFs and nanotwins may annihilate at the GB that forms after coalescence of 3C-SiC microcrystals generated by neighboring Si micropillars. Coalescence of adjacent 3C-SiC microcrystals results in the formation of twinned

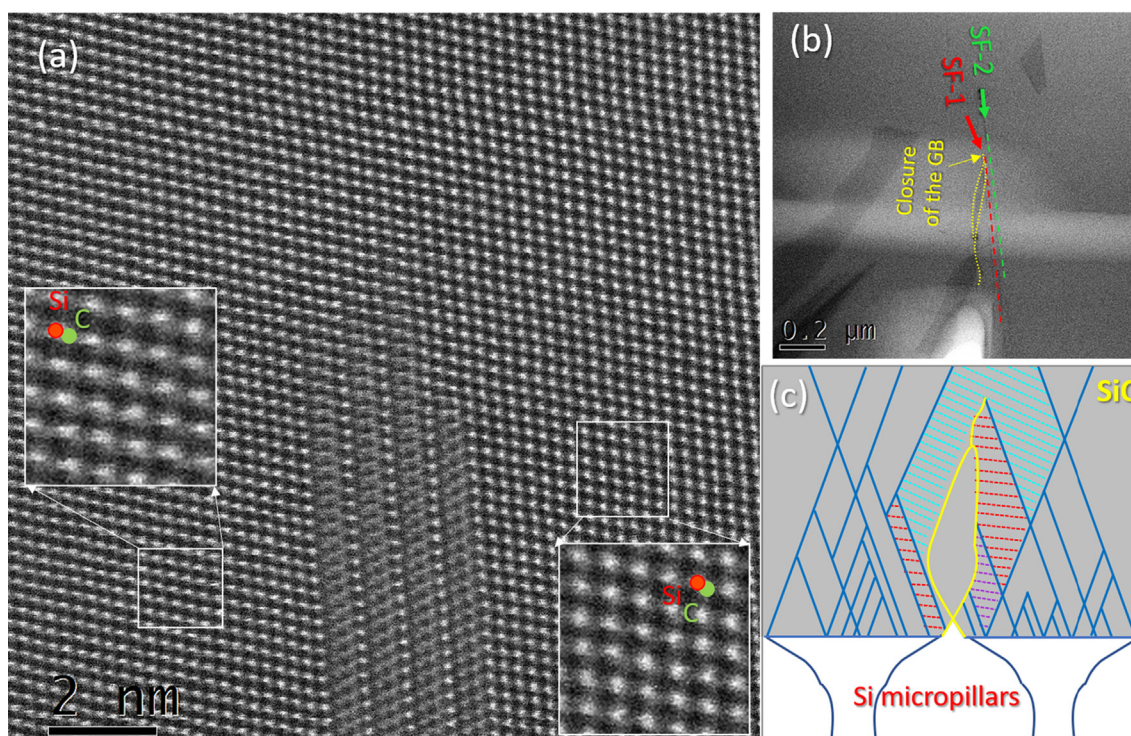


Fig. 11. (a) Atomic resolution HAADF-STEM image of the GB closure. (b) BF-STEM image of the region where the GB closure occurs. (c) Pictorial view explaining the mechanism of GB closure; the colored dashed lines indicate different crystallographic configurations.

- [38] A. Sarikov, A. Marzegalli, L. Barbisan, M. Zimbone, C. Bongiorno, M. Mauceri, D. Crippa, F. La Via, L. Miglio, Mechanism of stacking fault annihilation in 3C-SiC epitaxially grown on Si(001) by molecular dynamics simulations, *Cryst. Eng. Comm.* 23 (2021) 1566–1571, <https://doi.org/10.1039/DOCE01613F>.
- [39] N. Hatta, T. Kawahara, K. Yagi, H. Nagasawa, S. Reshanov, A. Schöner, Reliable Method for Eliminating Stacking Faults on 3C-SiC (001), *Mater. Sci. Forum* 717–720 (2012) 173–176, <https://doi.org/10.4028/www.scientific.net/MSF.717-720.173>.
- [40] P. Pirouz, J.W. Yang, Polytypic transformations in SiC: the role of TEM, *Ultramicroscopy* 51 (1993) 189–214, [https://doi.org/10.1016/0304-3991\(93\)90146-O](https://doi.org/10.1016/0304-3991(93)90146-O).